ACS APPLIED MATERIALS & INTERFACES

Research Article

www.acsami.org

Magnetism by Interfacial Hybridization and *p*-type Doping of MoS_2 in Fe_4N/MoS_2 Superlattices: A First-Principles Study

Nan Feng,[†] Wenbo Mi,*[,†] Yingchun Cheng,[‡] Zaibing Guo,[§] Udo Schwingenschlögl,[‡] and Haili Bai[†]

[†]Tianjin Key Laboratory of Low Dimensional Materials Physics and Preparation Technology, Institute of Advanced Materials Physics, Faculty of Science, Tianjin University, Tianjin 300072, China

[‡]PSE Division, and [§]Core Laboratories, King Abdullah University of Science and Technology (KAUST), Thuwal 23955-6900, Saudi Arabia

ABSTRACT: Magnetic and electronic properties of $Fe_4N(111)/MoS_2(\sqrt{3} \times \sqrt{3})$ superlattices are investigated by first-principles calculations, considering two models: (I) $Fe^{I}Fe^{II}$–S and (II) N–S interfaces, each with six stacking configurations. In model I, strong interfacial hybridization between Fe^{I}/Fe^{II} and S results in magnetism of monolayer MoS_2, with a magnetic moment of 0.33 μ_B for Mo located on top of Fe^{I}. For model II, no magnetism is induced due to weak N–S interfacial bonding, and the semiconducting nature of monolayer MoS_2 is preserved. Charge transfer between MoS_2 and N results in *p*-type MoS_2 with Schottky barrier heights of 0.5–0.6 eV. Our results demonstrate that the interfacial geometry and hybridization can be used to tune the magnetism and doping in $Fe_4N(111)/MoS_2(\sqrt{3} \times \sqrt{3})$ superlattices.

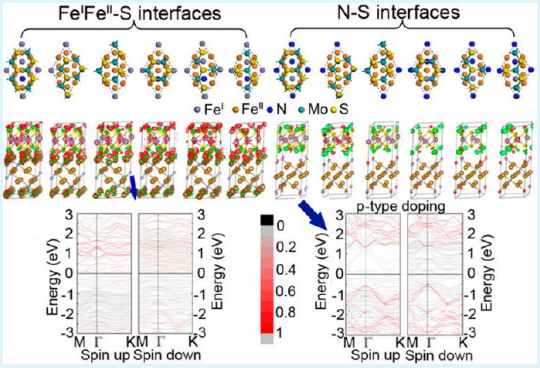

KEYWORDS: *MoS_2, Fe_4N, electronic structure, magnetic properties*

INTRODUCTION

Since the discovery of graphene, many studies have addressed two-dimensional materials.[1] Although the mobility of graphene can reach 1×10^5 $cm^2/(V\ s)$, lack of a band gap yields a small current on/off ratio that hampers its application in electronics devices.[2] Thus, two-dimensional materials with an intrinsic band gap are receiving more and more attention, such as monolayer MoS_2,[3−9] due to its high thermal stability, no dangling bonds, a direct band gap of 1.8 eV, and giant spin splitting in the K valleys, hence being of interest for electronics, photonics, spintronics, and valleytronics.[10,11] Recently a field-effect transistor based on monolayer MoS_2 with a high mobility of 200 $cm^2/(V\ s)$, current on/off ratio of 1×10^8, and ultralow standby power dissipation has been demonstrated.[12]

Mn, Fe, Co, and Zn doping in monolayer MoS_2 are predicted to result in two-dimensional diluted magnetic semiconductors.[13] However, as dilute doping is difficult experimentally, it is important to find other means to introduce magnetism in monolayer MoS_2. By the magnetic proximity effect,[14,15] spin injection from a high spin-polarized ferromagnetic electrode seems to be a promising route. Yet, it can be expected that the interfacial interaction plays a crucial role, compare, for example, the different barrier heights for electron tunneling in MoS_2/Au and MoS_2/Ti contacts,[16] *n*-doping of MoS_2 at Ir, Pd, and Ru interfaces,[17] controllable Schottky barrier heights in MoS_2/Co transistors,[18] and induced conductivity in MoS_2/Ti_2C.[19] To achieve high-temperature spintronics devices, electrodes with high spin polarization and Curie temperature are necessary. In bulk Fe_4N these quantities amount to almost −100% and 761 K,[20,21] respectively. In fact, magnetic tunnel junctions with Fe_4N electrodes are known for highly spin-polarized transport,[22,23] whereas Fe_4N/MoS_2 heterostructures have not been addressed so far. In this paper, we therefore study the electronic structures and magnetism of $Fe_4N(111)/MoS_2(\sqrt{3} \times \sqrt{3})$ superlattices by first-principles calculations and demonstrate that spin polarization is induced in monolayer MoS_2 in contact with Fe^{I}/Fe^{II} and p-type doping in contact with N.

CALCULATION DETAILS AND MODELS

Our first-principles calculations are based on density functional theory[24] and the projector augmented wave method[25] as implemented in Vienna Ab initio Simulation Package.[26] The Perdew–Burke–Ernzerhof[27] flavor of the spin-polarized generalized gradient approximation is used. The plane-wave cutoff is set to 500 eV and the Brillouin zone is sampled with $9 \times 9 \times 9$ and $9 \times 9 \times 1$ *k* meshes for bulk Fe_4N and the Fe_4N/MoS_2 superlattice, respectively. All structures are fully optimized until the force on each atom is less than 0.01 eV/Å and the total energy is converged to 1×10^{-5} eV.

Bulk Fe_4N has a cubic perovskite-type structure ($Pm3m$) with a lattice constant of a = 3.795 Å. Two types of Fe atoms (Fe^{I} and Fe^{II}) occupy the corner and face-centered sites, whereas N locates at the body-centered position. Fe^{I} is surrounded by 12 Fe^{II} atoms in a distance of $a/\sqrt{2}$ and Fe^{II}

Received: February 4, 2014
Accepted: February 27, 2014
Published: February 27, 2014

   dx.doi.org/10.1021/am500754p | *ACS Appl. Mater. Interfaces* 2014, 6, 4587–4594

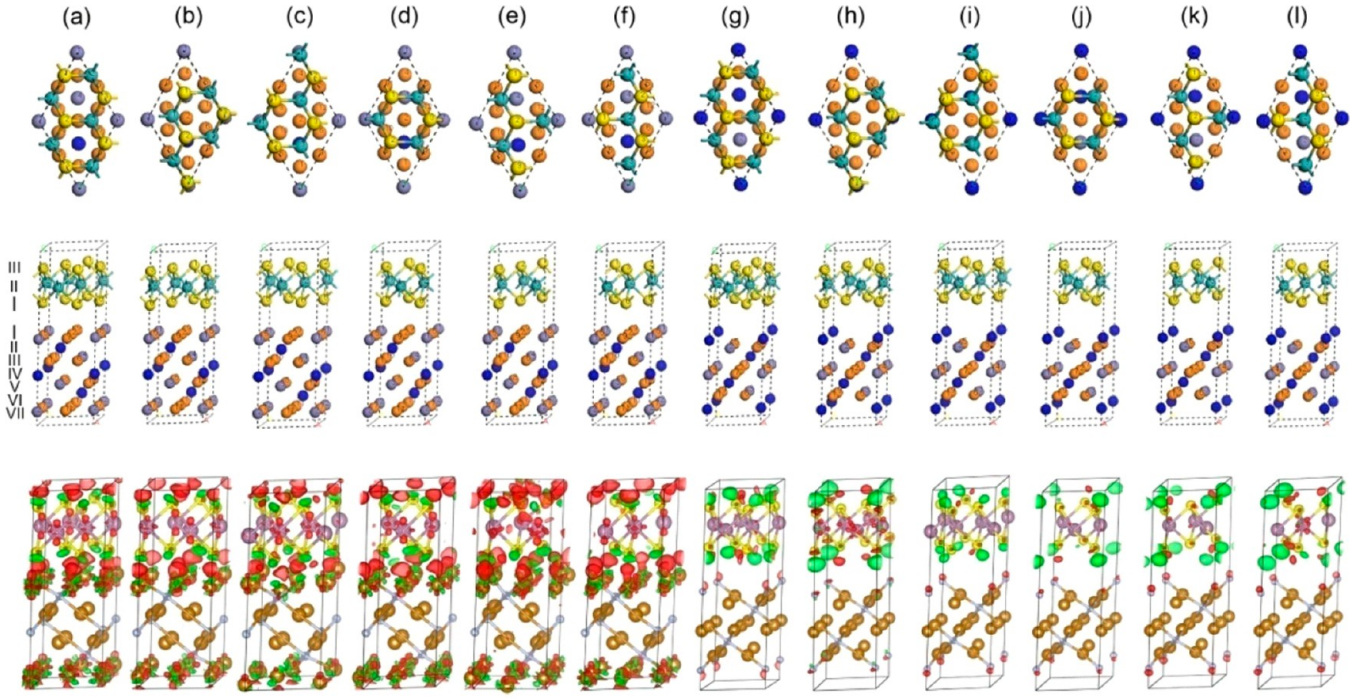

Figure 1. Top and side views as well as charge density difference. The red regions represent accumulation and the green regions depletion of electrons relative to the two isolated components. Light blue spheres stand for Fe^{I}, orange for Fe^{II}, navy blue for N, yellow for S, and cyan for Mo. (a–f) $Fe^{I}Fe^{II}$–S interface (0.0056 e/Å^3). (g–l) N–S interface (0.0002 e/Å^3).

has two N atoms in a distance of $a/2$ as the nearest neighbors and 12 Fe^{I} atoms as the second nearest neighbors.[28] Bulk MoS_2 is a layered semiconductor with space group $P63mmc$ (D_{6h} point group), consisting of stacked S–Mo–S monolayers with weak van der Waals interaction. The indirect band gap of 1.2 eV for bulk MoS_2 transforms into a direct band gap of 1.8 eV for monolayer MoS_2 (D_{3h} point group). The S–Mo–S slab consists of hexagonally arranged Mo atoms sandwiched between two sheets of likewise hexagonally arranged S atoms. In the sheets, the atoms are covalently bonded with S in a trigonal prismatic environment.

Fe_4N/MoS_2 superlattices are built by attaching a monolayer of MoS_2 on top of one unit cell (7 monolayers) of $Fe_4N(111)$. The surface unit cell of $Fe_4N(111)$ has $p(1 \times 1)$ periodicity with a lattice constant of 5.366 Å, whereas monolayer $MoS_2(0001)$ has $\sqrt{3} \times \sqrt{3}R30°$ periodicity with a lattice constant of 5.489 Å, resulting in a small lattice mismatch. Thus, an average in-plane lattice constant of 5.428 Å is adopted. We chose the Fe^{I}/Fe^{II} and N surfaces as terminations. By the periodic boundary conditions, the supercells contain two interfaces. Model I is the $Fe^{I}Fe^{II}$–S interface (see Figure 1a–f) and model II the N–S interface (see Figure 1g–l. To investigate how the electronic structure of monolayer MoS_2 depends on the interface geometry, we considered six stackings for each model, see Figure 1.

The stable pattern is determined by calculating the work of separation, i.e., the cohesive energy between Fe_4N and MoS_2, $W_{sep} = (E_{Fe_4N} + E_{MoS_2} - E_{Fe_4N/MoS_2})/2$, where E_{Fe_4N/MoS_2} is the total energy of the superlattice, E_{Fe_4N} and E_{MoS_2} represent the energies of the same supercell containing either the Fe_4N or MoS_2 parts (i.e., we keep the equilibrium structure obtained for the superlattice). The factor 2 accounts for the two interfaces present in the supercell. For illustrating the nature of the charge transfer at Fe_4N/MoS_2 interface, we calculate the charge density difference by subtracting the charge densities of the isolated MoS_2 and Fe_4N parts from the charge density of the superlattice. The electronic structures of isolated MoS_2 and Fe_4N are calculated by freezing the atoms of the respective component at the superlattice positions. The work function (W) is defined by the smallest energy required to remove an electron deep inside bulk crystal. It is defined as $W = V(\infty) - E_F$, where $V(\infty)$ is the electrostatic potential in the middle of the vacuum region of our supercells and E_F is the Fermi energy.

RESULTS AND DISCUSSION

For bulk Fe_4N a lattice constant of 3.795 Å is obtained, which agrees well with the experimental value.[20] The calculated average magnetic moments of Fe^{I}, Fe^{II}, and N are 2.95, 2.35, and 0.03 μ_B, respectively, in accordance with previous theoretical and experimental results.[29−33] Figure 2 presents the partial density of states (PDOS) for bulk Fe_4N and

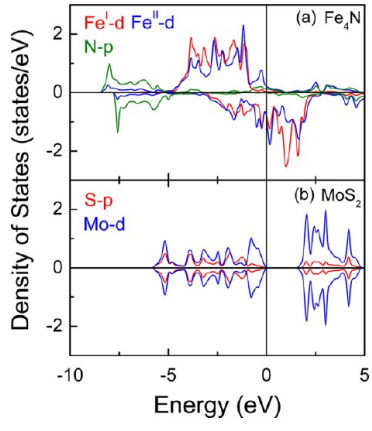

Figure 2. PDOS of (a) Fe_4N and (b) pristine monolayer MoS_2.

dx.doi.org/10.1021/am500754p | ACS Appl. Mater. Interfaces 2014, 6, 4587−4594

Table 1. Work of Separation W_{sep} (eV) and Optimized Bond Lengths d (Å) for Different Stackings, Compare Figure 1

model	case	W_{sep}	d_{FeI-S}	$d_{FeII(2)-S}$	$d_{FeII(5)-S}$	$d_{FeII(9)-S}$	d_{N-S}
Fe_4N/ MoS_2(I)	(a)	1.74	2.81	2.30	2.30	2.30	
	(b)	1.65	2.33	2.47	2.89	2.20	
	(c)	2.05	2.53	2.28	2.28	2.28	
	(d)	1.68	2.37	2.86	2.36	2.21	
	(e)	2.04	2.29	2.32	2.38	2.26	
	(f)	1.65	2.33	2.89	2.19	2.45	
Fe_4N/ MoS_2(II)	(g)	0.01					3.75
	(h)	0.01					3.59
	(i)	0.02					3.91
	(g)	0.02					3.76
	(k)	0.02					3.76
	(l)	0.02					3.64

Table 2. Optimized Lattice Constants and Bond Angles

case	a (Å)	b (Å)	c (Å)	α (deg)	β (deg)	γ (deg)
(a)	5.40	5.40	13.98	90.0	90.0	60.0
(b)	5.41	5.35	14.06	90.0	91.3	60.4
(c)	5.46	5.46	13.68	90.0	90.0	60.0
(d)	5.42	5.42	14.00	90.2	90.2	59.3
(e)	5.40	5.40	13.85	93.7	93.7	59.0
(f)	5.41	5.41	14.06	88.8	88.8	59.3
(g)	5.40	5.40	16.06	90.0	90.0	60.0
(h)	5.42	5.41	16.60	90.0	91.2	60.1
(i)	5.42	5.43	16.51	90.0	89.5	60.0
(j)	5.42	5.42	16.69	90.5	90.5	60.1
(k)	5.42	5.42	16.32	90.4	90.4	60.1
(l)	5.43	5.43	16.41	88.7	88.7	59.8

monolayer MoS_2. For Fe^I, Fe^{II}, and N (Figure 2a) a distinct spin splitting of Fe d states appears, which induces the ferromagnetism. The DOS of Fe_4N at E_F is mainly from the spin-down channel. From −8.5 to −5 eV the N p states strongly hybridize with Fe^{II} d states to form covalent bonds, whereas in the same energy range the Fe^I d states show hardly any hybridization with N. Thus, Fe^{II} magnetic moment is smaller than that of Fe^I. The band structure of monolayer MoS_2 (1 × 1 unit cell) shows a direct band gap of 1.7 eV between the valence band (VB) maximum and conduction band (CB) minimum at K point of Brillouin zone, consistent with previous theoretical works[13,34,35] and photoluminescence spectroscopy.[36] Figure 2b indicates strong hybridization between the Mo d and S p states in the VB and CB, where the VB maximum and CB minimum are governed by Mo d states.

In Table 1, the work of separation and optimized bond lengths are presented for different stackings. Monolayer MoS_2 strongly interacts with Fe^IFe^{II}-terminated surface, forming chemical bonds with significant configuration dependence. The stability order in model I is found to be b < f < d < a < e < c, see Figure 1. The energetically favorable case is c, i.e., Mo located on top of Fe^I. The large W_{sep} = 2.05 eV is explained by strong Fe^{II}−S bonds with a bond length of 2.28 Å. In contrast, for MoS_2 on the N-terminated surface the results indicate that the interaction is rather weak and fairly insensitive to the stacking. The optimized distances and bond angles point to strong distortions of MoS_2 and Fe_4N, where the S atoms either are pulled toward Fe_4N or pushed away, see Tables 1 and 2, which lowers the symmetry of Fe_4N.

We first focus on model I to explore the variations of the electronic structure induced by the interfacial coupling. As compared to the value of bulk Fe_4N, the magnetic moments decrease by 4.4, 4.8, 3.7, 3.1, 3.4, and 4.9% for cases a−f, respectively.

Usually, the appearance of Fe magnetic moments in Fe_4N is ascribed to symmetry breaking, as N is located at the body-centered site of the nonmagnetic face-centered cubic unit cell of Fe. So, the enhancement of the Fe magnetic moments in our

Table 3. Average Fe^I and Fe^{II} Magnetic Moments $\bar{m}(\mu_B)$ for Each Fe_4N Layer in Model I; Magnetic Moments $m(\mu_B)$ of Fe^I, Fe^{II}, and N at the Interfaces As Well as of S and Mo

moment	atom		bulk	a	b	c	d	e	f
$\bar{m}$	Fe^I	layer I	2.95	2.83	2.74	2.82	2.80	2.68	2.76
		layer III	2.95	2.90	2.87	2.83	2.88	2.88	2.87
		layer V	2.95	2.90	2.87	2.84	2.89	2.87	2.87
		layer VII	2.95	2.84	2.75	2.82	2.80	2.75	2.75
	Fe^{II}	layer I	2.35	2.28	2.29	2.27	2.33	2.35	2.27
		layer III	2.35	2.21	2.20	2.28	2.25	2.24	2.20
		layer V	2.35	2.21	2.20	2.28	2.25	2.23	2.20
		layer VII	2.35	2.28	2.29	2.27	2.32	2.35	2.31
m	Fe^I (1,2)		2.95	2.83	2.74	2.82	2.80	2.68	2.76
	Fe^{II} (2)		2.35	2.27	2.53	2.27	2.58	2.46	2.59
	Fe^{II} (5)		2.35	2.24	2.59	2.27	2.43	2.27	1.67
	Fe^{II} (9)		2.35	2.31	1.73	2.26	1.99	2.32	2.53
	N (2)		0.03	−0.03	−0.03	−0.02	−0.02	−0.01	−0.03
	S(1)		0	0.02	0.02	0.03	0.02	0.02	0.02
	S(2)			0.03	0.01	0.03	0.01	0.03	0.02
	S(3)			0.03	0.01	0.03	0.02	0.02	0.01
	S(4)			0.03	0.01	0.03	0.01	0.01	0.01
	S(5)			0.02	0.02	0.03	0.02	0.03	0.01
	S(6)			0.03	0.02	0.03	0.02	0.02	0.02
	Mo(1)			−0.03	−0.09	0.22	−0.04	−0.04	−0.09
	Mo(2)			0.03	0.07	−0.03	0.00	−0.04	0.07
	Mo(3)			−0.02	−0.09	−0.03	0.01	−0.16	−0.09

dx.doi.org/10.1021/am500754p | ACS Appl. Mater. Interfaces 2014, 6, 4587−4594

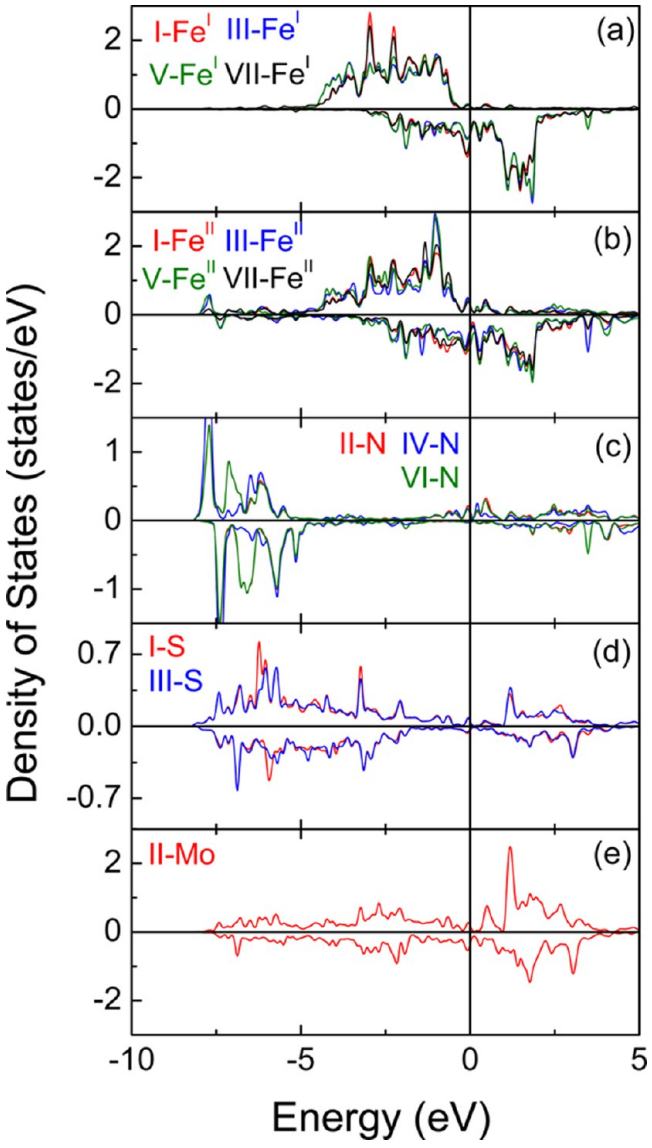

Figure 3. PDOS of the fully relaxed case a of the Fe_4N/MoS_2 superlattice: (a) Fe^{I}, (b) Fe^{II}, (c) N, (d) S, and (e) Mo. The Fermi energy is indicated by vertical lines and is set to 0 eV.

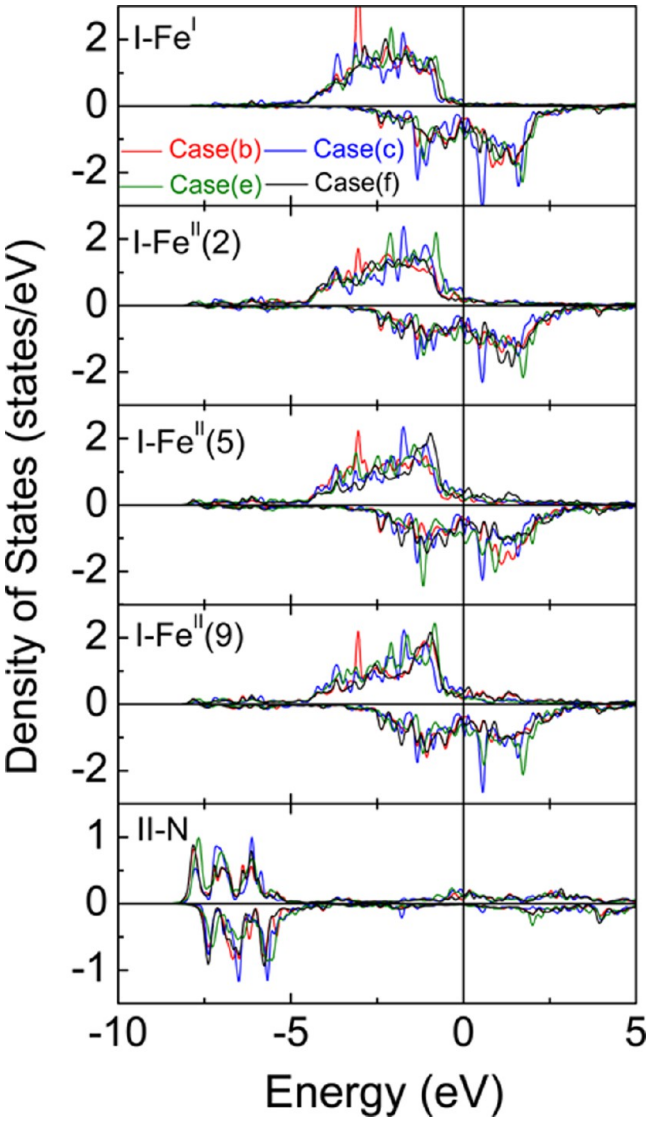

Figure 4. PDOS of Fe_4N in the fully relaxed Fe_4N/MoS_2 superlattice for model I, cases b, c, e, and f. The rows represent Fe^{I} and Fe^{II} in layer I and N in layer II. The Fermi energy is indicated by vertical lines.

case should also be related to the symmetry. Since they mainly originate from unpaired d electrons and the enhanced hybridization between Fe and other atoms reduces the amount of unpaired d electrons, it is the hybridization that determines the spin polarization.[37] The average Fe^{I} and Fe^{II} magnetic moments for each Fe_4N layer in model I are shown in Table 3.

We take case a as an example to illustrate the similarities among the different stackings, see the PDOSs in Figure 3. The label I−Fe^{II}, for example, refers to layer I, as defined in Figure 1, and Fe^{II} denotes the Fe atoms at face-centered sites (distinguished by numbers in round brackets). Reduced Fe^{I} magnetic moments in layers I and VII are attributed to hybridization with S in layers I, III and enhanced hybridization with N in layers II, VI, respectively. Fe^{I} magnetic moments in layers III and V decrease due to enhanced hybridization with N in layers II, IV and IV, VI, respectively. As Fe^{I} in layers I and VII strongly hybridize with S, the Fe^{I} magnetic moments are slightly smaller than in layers III and V. The average Fe^{II} magnetic moment for each layer is smaller than the bulk value except for layers I and VII in case e, see Table 3. The Fe^{II} atoms in layers I and VII hybridize with S in layers I, III and N in layers II, VI, respectively, which reduces the magnetic moment. The enhanced hybridization between Fe^{II} in layers III, V and N in layers II, IV, VI lowers the magnetic moment. Except for case c, the Fe^{II} magnetic moments in layers I and VII are slightly enhanced as compared to layers III and V because of stronger hybridization with N than S.

To highlight the influence of the stacking, we select cases b, c, e, and f as examples. Fe_4N layers I and VII are identical due to the periodicity of the supercell. The PDOSs in Figure 4 are obtained by projecting on the Fe^{I}, Fe^{II}, and N atoms at the interface, see Table 3 for corresponding magnetic moments. The smaller/larger Fe^{I} magnetic moments in case e/c are a consequence of the stronger/weaker hybridization with S just below E_F. Three Fe^{II} magnetic moments appear in layer I in cases b, e, and f, reflecting different hybridizations with S. Whereas the broken symmetry at the interface[38] promotes the Fe^{II} magnetic moment in layer I, the stronger hybridization between Fe^{II} and S weakens it. For case b, we find the strongest

dx.doi.org/10.1021/am500754p | ACS Appl. Mater. Interfaces 2014, 6, 4587−4594

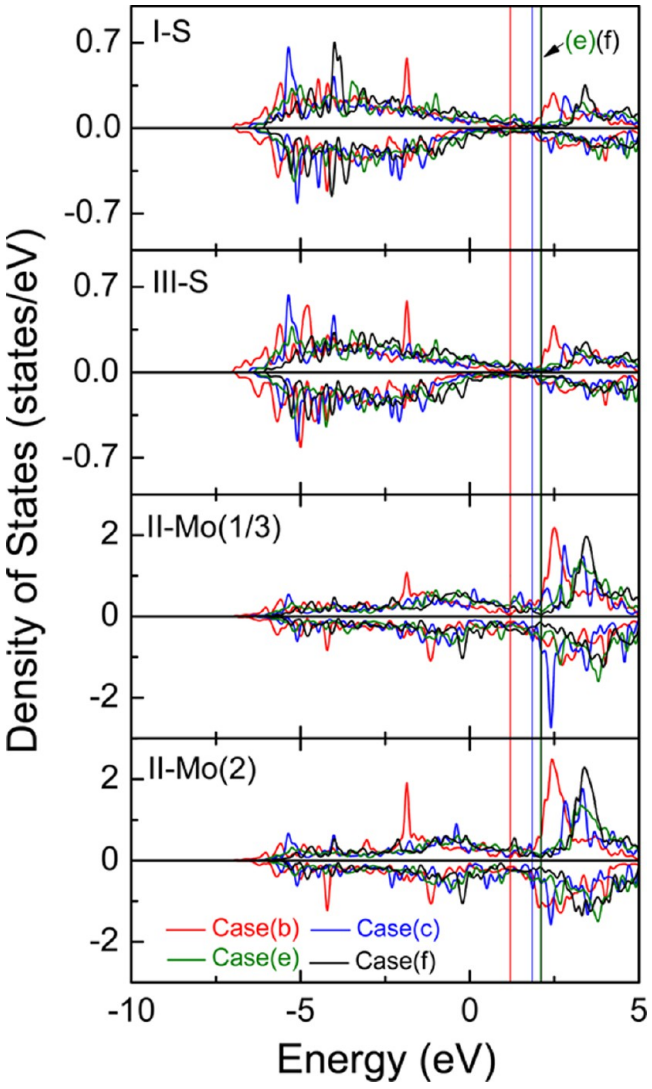

Figure 5. PDOS of MoS_2 in the fully relaxed Fe_4N/MoS_2 superlattice for model I, cases b, c, e, and f. The Fermi energy is indicated by vertical lines.

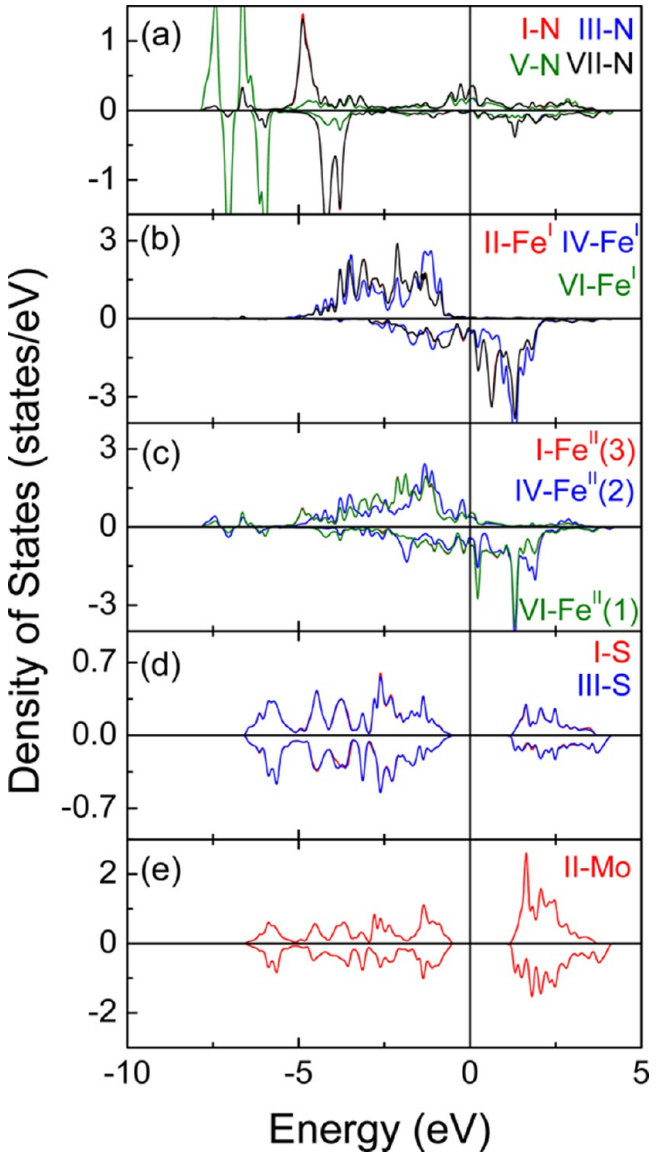

Figure 6. PDOS of the fully relaxed case g of the Fe_4N/MoS_2 superlattice: (a) N, (b) Fe^{I}, (c) Fe^{II}, (d) S, and (e) Mo. The Fermi energy is indicated by vertical lines.

hybridization with S in layer I for $Fe^{II}(9)$ followed by $Fe^{II}(2)$ and $Fe^{II}(5)$. For case c, the PDOS of the three Fe^{II} atoms in layer I is almost the same, reflecting a similar interaction with

Table 4. Average Fe^{I} and Fe^{II} Magnetic Moments $\bar{m}(\mu_B)$ for Each Fe_4N Layer in Model II; Magnetic Moments $m(\mu_B)$ of Fe^{I}, Fe^{II}, and N at the Interfaces As Well As Band Gaps E_g(eV) and *p*-Type Schottky Barrier Heights $\Phi_{B,p}$(eV)

moment/energy	atom		bulk	g	h	i	j	k	l
$\bar{m}$	Fe^{I}	layer II	2.95	2.98	2.99	2.03	2.98	2.98	2.99
		layer IV	2.95	2.95	2.94	2.26	2.93	2.93	2.94
		layer VI	2.95	2.98	2.99	2.05	2.98	2.98	2.99
	Fe^{II}	layer II	2.35	2.17	2.12	2.27	2.05	2.05	2.12
		layer IV	2.35	2.19	2.28	2.28	2.26	2.26	2.28
		layer VI	2.35	2.17	2.12	2.28	2.02	2.02	2.12
m	Fe^{I}	(2)	2.95	2.98	2.99	2.98	2.98	2.98	2.99
	Fe^{II}	(3)	2.35	2.15	2.01	2.23	1.96	1.96	2.32
		(5)	2.35	2.24	2.32	1.93	2.29	2.29	2.05
		(8)	2.35	2.13	2.02	1.92	1.90	1.90	2.00
	N	(1,2)	0.03	−0.01	−0.02	−0.03	−0.03	−0.03	−0.02
E_g				1.89	1.87	1.86	1.87	1.86	1.86
$\Phi_{B,p}$				0.54	0.54	0.59	0.59	0.59	0.54

dx.doi.org/10.1021/am500754p | ACS Appl. Mater. Interfaces 2014, 6, 4587−4594

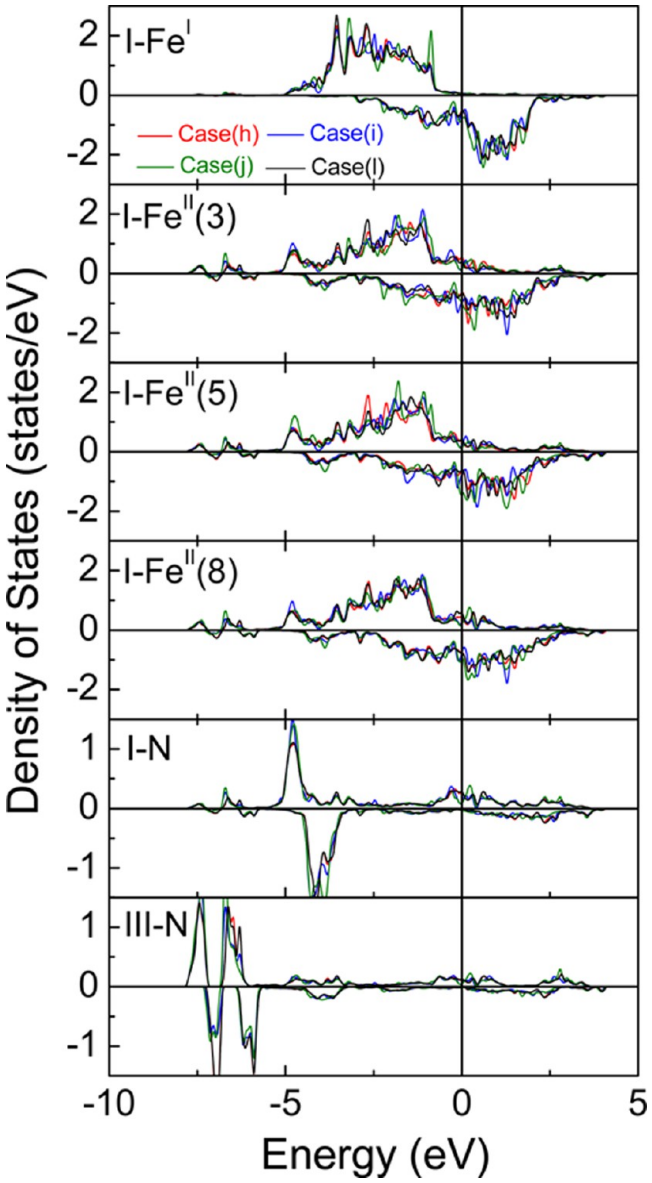

Figure 7. PDOS of Fe_4N in the fully relaxed Fe_4N/MoS_2 superlattice for model II, cases h, i, j, and l. The rows represent Fe^{I} and Fe^{II} in layer I and N in layers I and III, respectively. The Fermi energy is indicated by vertical lines.

MoS_2, whereas in case e S hybridizes more with $Fe^{II}(5)$ than with $Fe^{II}(9)$ and even less with $Fe^{II}(2)$, as shown in Figures 4 and 5. This order is the same in case f, in which the hybridization of $Fe^{II}(5)/Fe^{II}(9)$ with S is smaller/larger than in all other cases.

Figure 5 gives Mo and S PDOSs for model I. It is clear that the electronic states of S are similar in layers I and III, where the interaction with Fe_4N has dramatic effects near E_F. Strong orbital overlap between Fe^{I}, Fe^{II}, S, and Mo induces metallicity in MoS_2. The bonds between S (layer I) and Fe^{I}/Fe^{II} (layer I) weaken the Mo−S bonds, which leads to the spin polarization with a small Mo magnetic moment, see Table 3. Clearly, the magnetic moments depend on the position, with the highest value of 0.22 μ_B in case c, where Mo sits directly on top of Fe^{I}. The total magnetic moments of MoS_2 are 0.14, −0.02, 0.33, 0.10, −0.11, and −0.02 μ_B in cases a−f. Denoting the total DOS in the spin-up and spin-down channels by $N_\uparrow$ and $N_\downarrow$, the spin polarization $P = [N_\uparrow(E_F) - N_\downarrow(E_F)]/[N_\uparrow(E_F) + N_\downarrow(E_F)]$ can be derived from Figure 5 as P = −40, −52, −52, and −44%. The fact that the sign is the same as in Fe_4N demonstrates that the polarization is not inverted.

The charge transfer at the interfaces is quantified by charge density difference calculations (see Figure 1), showing that charge is lost from the Fe and S atoms, while it accumulates in the Fe−S bond region, reflecting covalent bonding across the interface. It is worth noting that some extra charge accumulates around Mo. We find more charge in the covalent Fe^{I}−S bonds for case e as compared to all other cases, consistent with the shortest bond length (Table 1) and the smallest Fe^{I} magnetic moment [Table 3]. For cases a and c, the charge distributions between Fe^{II} and S in layer I are almost identical (same Fe^{II} magnetic moment), whereas in cases b, e, and f the amount of charge accumulated in the Fe^{II}−S bonds corresponds perfectly to our previous analysis of Fe^{II} magnetic moments. The stronger the covalent bond is, the smaller the Fe^{II} magnetic moment is.

For model II the Fe_4N magnetic moments are subject to reductions of 5.14, 5.42, 7.40, 7.42, 7.42, and 5.36% as compared to bulk Fe_4N for cases g−l, respectively. The obtained average Fe^{I} and Fe^{II} magnetic moments are presented in Table 4. The electronic properties of MoS_2 are similar for the different stackings due to similar interactions with Fe_4N. We select case g as an example to elaborate on the similarities in Figure 6. Hybridization appears between N in layer I and S in layer I, whereas Fe has hardly any hybridization with S because of the large distance. As compared to model I, the Fe^{I} magnetic moment in layers II and VI is larger than bulk value. The Fe^{II} magnetic moment, on the other hand, is smaller, where the reduced values in layers II and VI can be ascribed to the enhanced hybridization with N in layers I, III, V, and VII. The weak interfacial bonds induce no significant Mo and S magnetic moments (0.001 μ_B).

As cases k and j behave similarly, we use cases h, i, j and l to study the stacking effect. The magnetic moments of Fe^{I}, Fe^{II}, and N at the interfaces in model II are shown in Table 4. The three values of Fe^{II} magnetic moments in layer II reflect different hybridizations with N in layers I and III. From Figure 7, there is less hybridization between $Fe^{II}(5)$ and N in layers I and III (larger magnetic moment) in case h, as compared to $Fe^{II}(3)$ and $Fe^{II}(8)$. In case i $Fe^{II}(3)$ shows the smallest hybridization with N in layer III, while all Fe^{II} atoms interact similarly with N atoms in layer I, as shown in Figure 7. Similarly, in case j, the enhanced $Fe^{II}(5)$ magnetic moment is due to reduced hybridization with N in layer III. The interaction with layer I is almost the same for all the Fe^{II} atoms. Finally, case l resembles case i.

Figure 8 gives band structures for pristine monolayer MoS_2 and the superlattices, demonstrating the changes in the electronic states of MoS_2 upon interface formation. In Figure 8a, the original K point of the 1 × 1 unit cell of monolayer MoS_2 is folded to the Γ point of the $\sqrt{3} \times \sqrt{3}$ cell. In case c the MoS_2 bands strongly hybridize with Fe_4N, inducing a metallic character of monolayer MoS_2, as shown in Figure 8b, c. For case g, although MoS_2 hybridizes with Fe_4N to a certain extent, the gross characters of the MoS_2-related bands are almost identical to the free-standing monolayer, see Figure 8d, e, indicating a weak interaction. Furthermore, in case g E_F is located 0.56 eV above the VB maximum and 1.37 eV below the CB minimum of MoS_2, indicating p-doping. In model II, interestingly, the semiconducting nature of monolayer MoS_2 is

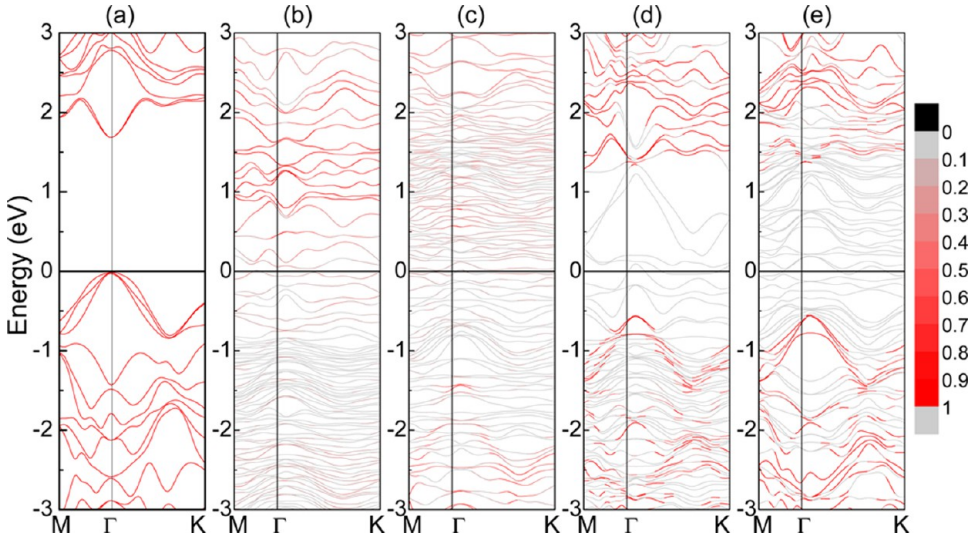

Figure 8. (a) Band structure of a $\sqrt{3} \times \sqrt{3}$ superlattice of monolayer MoS_2. (b, d) Majority and (c, e) minority spin band structure for cases (b, c) c and (d, e) g. Red color indicates MoS_2 and gray Fe_4N. The Fermi energy is indicated by vertical lines.

preserved. The band gap increases as compared to model I, see Table 4.

Because E_F lies in the MoS_2 band gap, a Schottky barrier is formed at the interface for model II, which is of crucial importance for the device performance. The p-type Schottky barrier heights ($\Phi_{B,p}$) are the energy differences between the VB maximum of MoS_2 and E_F of the superlattice. We obtain values of 0.54, 0.54, 0.59, 0.59, 0.59, and 0.54 eV for cases g–l, respectively (Table 4). An ideal Schottky junction fulfills $\Phi_{B,p} = E_g - (\Phi_M - \chi_s)$, where E_g and χ_s are the band gap and electron affinity of the semiconductor and Φ_M is the work function of the metal.[39] From the vacuum potential and E_F, we obtain Φ_M = 5.38 eV for the N-terminated surface of $Fe_4N(111)$. We derive χ_s = 4.27 eV, which is identical to a reported value.[17] The resulting $\Phi_{B,p}$ = 0.57 eV deviates only slightly from the value derived from the band structure, reflecting weak Fermi level pinning and proximity to the Schottky limit. In general, Fermi level pinning is governed by metal induced gap states,[40] surface states,[41] and dipole effects.[42] Figure 1 shows significant charge accumulation around the interfacial N atoms and charge depletion at S atoms. Therefore, the p-type doping of MoS_2 on the N-terminated surface of $Fe_4N(111)$ is due to electron transfer from MoS_2 to Fe_4N. Even in cases h and j, where the charge is more localized, there is a transfer to N.

CONCLUSION

The main findings of our first-principles calculations on $Fe_4N(111)/MoS_2(\sqrt{3} \times \sqrt{3})$ superlattices are summarized as follows: For model I: (1) strong Fe–S chemical bonds are formed; (2) the Fe^I and Fe^{II} magnetic moments in the Fe_4N region are reduced; (3) spin-polarization is induced in MoS_2, with the largest magnetic moments of 0.33 μ_B for Mo located on top of the interfacial Fe^I atoms. For model (II): (1) interfacial N–S bonding is relatively weak; (2) the Fe^{II} magnetic moments are reduced; (3) the semiconducting nature of MoS_2 is preserved and the band gap increases. Importantly, we find p-type doping of MoS_2 with Schottky barrier heights in the range of 0.5–0.6 eV for different stackings. Therefore, Fe-terminated Fe_4N in contact with monolayer MoS_2 has potential in spintronics devices, whereas N-termination is interesting for high-performance p-type field effect transistors.

AUTHOR INFORMATION

Corresponding Author

*E-mail: miwenbo@tju.edu.cn.

Author Contributions

N.F. and W.M. designed the outline of the manuscript and wrote the main manuscript text. Y.C., Z.G., U.S., and H.B. contributed detailed discussions and revisions. All authors reviewed the manuscript.

Notes

The authors declare no competing financial interest.

ACKNOWLEDGMENTS

W.B.M. was supported by the National Natural Foundation of China (51172126), Key Project of Natural Foundation of Tianjin City (12JCZDJC27100), Program for New Century Excellent Talents in University (NCET-13-0409), and Scientific Research Foundation for the Returned Overseas Chinese Scholars, State Education Ministry of China. Y.C.C. and U.S. were supported by a CRG grant of KAUST.

REFERENCES

(1) Novoselov, K. S.; Geim, A. K.; Morozov, S. V.; Jiang, D.; Zhang, Y.; Dubonos, S. V.; Grigorieva, I. V.; Firsov, A. A. Electric Field Effect in Atomically Thin Carbon Films. *Science* **2004**, *306*, 666–669.

(2) Schwierz, F. Graphene Transistors. *Nat. Nanotechnol.* **2010**, *5*, 487–496.

(3) Novoselov, K.; Jiang, D.; Schedin, F.; Booth, T.; Khotkevich, V.; Morozov, S.; Geim, A. Two-Dimensional Atomic Crystals. *Proc. Natl. Acad. Sci. U.S.A.* **2005**, *102*, 10451–10453.

(4) Mak, K. F.; He, K.; Shan, J.; Heinz, T. F. Control of valley Polarization in Monolayer MoS_2 by Optical Helicity. *Nat. Nanotechnol.* **2012**, *7*, 494–498.

(5) Mak, K. F.; Lee, C.; Hone, J.; Shan, J.; Heinz, T. F. Atomically Thin MoS_2: a New Direct-Gap Semiconductor. *Phys. Rev. Lett.* **2010**, *105*, 136805.

(6) Liu, K. K.; Zhang, W. J.; Lee, Y. H.; Lin, Y. C.; Chang, M. T.; Su, C. Y.; Chang, C. S.; Li, H.; Shi, Y. M.; Zhang, H.; Lai, C. S.; Li, L. J. Growth of Large-Area and Highly Crystalline MoS_2 Thin Layers on Insulating Substrates. *Nano Lett.* **2012**, *12*, 1538–1544.

(7) Han, S. W.; Kwon, H.; Kim, S. K.; Ryu, S.; Yun, W. S.; Kim, D. H.; Hwang, J. H.; Kang, J. S.; Baik, J.; Shin, H. J.; Hong, S. C. Band-

Gap Transition Induced by Interlayer Van der Waals Interaction in MoS_2. *Phys. Rev. B* **2011**, *84*, 045409.
(8) Zeng, H.; Dai, J.; Yao, W.; Xiao, D.; Cui, X. Valley Polarization in MoS_2 Monolayers by Optical Pumping. *Nat. Nanotechnol.* **2012**, *7*, 490−493.
(9) Li, Y.; Wang, H.; Xie, L.; Liang, Y.; Hong, G.; Dai, H. MoS_2 Nanoparticles Grown on Graphene: An Advanced Catalyst for the Hydrogen Evolution Reaction. *J. Am. Chem. Soc.* **2011**, *133*, 7296−7299.
(10) Zhu, Z. Y.; Cheng, Y. C.; Schwingenschlögl, U. Giant Spin-Orbit-Induced Spin Splitting in Two-Dimensional Transition-Metal Dichalcogenide Semiconductors. *Phys Rev. B* **2011**, *84*, 153402.
(11) Ohno, Y.; Terauchi, R.; Adachi, T.; Matsukura, F.; Ohno, H. Spin Relaxation in GaAs(110) Quantum Wells. *Phys. Rev. Lett.* **1999**, *83*, 4196−4199.
(12) Radisavljevic, B.; Radenovic, A.; Brivio, J.; Giacometti, V.; Kis, A. Single-Layer MoS_2 Transistors. *Nat. Nanotechnol.* **2011**, *6*, 147−150.
(13) Cheng, Y. C.; Zhu, Z. Y.; Mi, W. B.; Guo, Z. B.; Schwingenschlögl, U. Prediction of Two-Dimensional Diluted Magnetic Semiconductors: Doped Monolayer MoS_2 Systems. *Phys. Rev. B* **2013**, *87*, 100401(R).
(14) Eremeev, S. V.; Menshov, V. N.; Tugushev, V. V.; Echenique, P. M.; Chulkov, E. V. Magnetic Proximity Effect at the Three-Dimensional Topological Insulator/Magnetic Insulator Interface. *Phys. Rev. B* **2013**, *88*, 144430.
(15) Vobornik, I.; Manju, U.; Fujii, J.; Borgatti, F.; Torelli, P.; Krizmancic, D.; Hor, Y. S.; Cava, R. J.; Panaccione, G. Magnetic Proximity Effect As a Pathway to Spintronic Applications of Topological Insulators. *Nano Lett.* **2011**, *11*, 4079−4082.
(16) Popov, I.; Seifert, G.; Tománek, D. Designing Electrical Contacts to MoS_2 Monolayers: A Computational Study. *Phys. Rev. Lett.* **2012**, *108*, 156802.
(17) Chen, W.; Santos, E. J. G.; Zhu, W. G.; Kaxiras, E.; Zhang, Z. Y. Tuning the Electronic and Chemical Properties of Monolayer MoS_2 Adsorbed on Transition Metal Substrates. *Nano Lett.* **2013**, *13*, 509−514.
(18) Chen, J. R.; Odenthal, P. M.; Swartz, A. G.; Floyd, G. C.; Wen, H.; Luo, K. Y.; Kawakami, R. K. Control of Schottky Barriers in Single Layer MoS_2 Transistors with Ferromagnetic Contacts. *Nano Lett.* **2013**, *13*, 3106−3110.
(19) Gan, L. Y.; Zhao, Y. J.; Huang, D.; Schwingenschlögl, U. First-Principles Analysis of MoS_2/Ti_2C and MoS_2/Ti_2CY_2 (Y = F and OH) All-2D Semiconductor/Metal Contacts. *Phys. Rev. B* **2013**, *87*, 245307.
(20) Kokado, S.; Fujima, N.; Harigaya, K.; Shimizu, H.; Sakuma, A. Theoretical Analysis of Highly Spin-Polarized Transport in the Iron Nitride Fe_4N. *Phys. Rev. B* **2006**, *73*, 172410.
(21) Nagakura, S. Electronic Structure of Iron Nitrides Studied by Electron Diffraction. I. γ'-Fe_4N. *J. Phys. Soc. Jpn.* **1968**, *25*, 488−498.
(22) Sunaga, K.; Tsunoda, M.; Komagaki, K.; Uehara, Y.; Takahashi, M. Inverse Tunnel Magnetoresistance in Magnetic Tunnel Junctions with an Fe_4N Electrode. *J. Appl. Phys.* **2007**, *102*, 013917.
(23) Tsunoda, M.; Komasaki, Y.; Kokado, S.; lsogami, S.; Chen, C. C.; Takahasi, M. Negative Anisotropic Magnetoresistance in Fe_4N Film. *Appl. Phys. Express* **2009**, *2*, 083001.
(24) Kohn, W.; Sham, L. J. Self-Consistent Equations Including Exchange and Correlation Effects. *Phys. Rev.* **1965**, *140*, A1133−A1138.
(25) Blöchl, P. E. Projector Augmented-Wave Method. *Phys. Rev. B* **1994**, *50*, 17953−17979.
(26) Kresse, G.; Furthmüller, J. Efficient Iterative Schemes for Ab Initio Total-Energy Calculations Using a Plane-Wave Basis Set. *Phys. Rev. B* **1996**, *54*, 11169−11186.
(27) Perdew, J. P.; Burke, K.; Ernzerhof, M. Generalized Gradient Approximation Made Simple. *Phys. Rev. Lett.* **1996**, *77*, 3865−3868.
(28) Mohn, P.; Mater, S. F. The γ'-Fe_4N System Revisited: An Ab Initio Calculation Study of the Magnetic Interactions. *J. Magn. Magn. Mater.* **1999**, *191*, 234−240.
(29) von Appen, J.; Dronskowski, R. Predicting New Ferromagnetic Nitrides from Electronic Structure Theory: $IrFe_3N$ and $RhFe_3N$. *Angew. Chem., Int. Ed.* **2005**, *44*, 1205−1210.
(30) Coehoorn, R.; Daalderop, G. H. O.; Jansen, H. J. F. Full-potential calculations of the magnetization of $Fe_{16}N_2$ and Fe_4N. *Phys. Rev. B* **1993**, *48*, 3830−3834.
(31) Zhao, E. J.; Xiang, H. P.; Meng, J.; Wu, Z. J. First-Principles Investigation on the Elastic, Magnetic and Electronic Properties of MFe_3N (M = Fe, Ru, Os). *Chem. Phys. Lett.* **2007**, *449*, 96−100.
(32) Lv, Z. Q.; Gao, Y.; Sun, S. H.; Qv, M. G.; Wang, Z. H.; Shi, Z. P.; Fu, W. T. Electronic, Magnetic and Elastic Properties of γ'-Fe_4X (X = B/C/N) from Density Functional Theory Calculations. *J. Magn. Magn. Mater.* **2013**, *333*, 39−45.
(33) Frazer, B. C. Magnetic Structure of Fe_4N. *Phys. Rev.* **1958**, *112*, 751−754.
(34) Li, Y. F.; Zhou, Z.; Zhang, S. B.; Chen, Z. F. MoS_2 Nanoribbons: High Stability and Unusual Electronic and Magnetic Properties. *J. Am. Chem. Soc.* **2008**, *130*, 16739−16744.
(35) Lebègue, S.; Eriksson, O. Electronic Structure of Two-Dimensional Crystals from Ab Initio theory. *Phys. Rev. B* **2009**, *79*, 115409.
(36) Splendiani, A.; Sun, L.; Zhang, Y. B.; Li, T. S.; Kim, J.; Chim, C. Y.; Galli, G.; Wang, F. Emerging Photoluminescence in Monolayer MoS_2. *Nano Lett.* **2010**, *10*, 1271−1275.
(37) Shi, Y. J.; Du, Y. L.; Chen, G. Ab Initio Study of Structural and Magnetic Properties of Cubic Fe_4N (001) Surface. *Solid State Commun.* **2012**, *152*, 1581−1584.
(38) Shen, Y. R. Optical Second Harmonic Generation at Interfaces. *Annu. Rev. Phys. Chem.* **1989**, *40*, 327−350.
(39) Cowley, A. M.; Sze, S. M. Surface States and Barrier Height of Metal−Semiconductor Systems. *J. Appl. Phys.* **1965**, *36*, 3212−3220.
(40) Tersoff, J. Schottky barrier heights and the continuum of gap states. *Phys. Rev. Lett.* **1984**, *52*, 465−468.
(41) Geppert, D. V.; Cowley, A. M.; Dore, B. V. Correlation of Metal−Semiconductor Barrier Height and Metal Work Function; Effects of Surface States. *J. Appl. Phys.* **1966**, *37*, 2458−2467.
(42) Tung, R. T. Formation of an Electric Dipole at Metal−Semiconductor Interfaces. *Phys. Rev. B* **2001**, *64*, 205310.